Silver nanopillar coatings grown by glancing angle magnetron sputtering for reducing multipactor effect in spacecrafts

G. Troncoso[a], J.M. García-Martín[b], M.U. González[b], C. Morales[a], M. Fernández-Castro[b], J. Soler-Morala[b], L. Galán[a], L. Soriano[a,*]

[a)] *Departamento de Física Aplicada and Instituto Nicolás Cabrera, Universidad Autónoma de Madrid (CEI UAM+CSIC), Francisco Tomás y Valiente 7, E-28049 Madrid, Spain.*

[b)] *Instituto de Micro y Nanotecnología, IMN-CNM, CSIC (CEI UAM+CSIC), Isaac Newton 8, E-28760 Tres Cantos, Madrid. Spain*

[*]*CorrespondingAuthor: l.soriano@uam.es*

Keywords: secondary electron emission; anti-multipactor coatings; Ag nanopillars; glancing angle deposition; magnetron sputtering;

Abstract:

We have studied nanometric high aspect ratio Ag nanopillar coatings exhibiting reduced secondary electron emission for the mitigation of multipactor effect in radio-frequency space devices of high frequency and high power. The Ag nanopillars have been grown by glancing angle deposition with DC magnetron sputtering. Some samples have been covered by a gold capping layer to reduce oxidation and aging effects. The secondary emission yield of the surfaces of these samples has been measured and compared to those of flat Ag and Au reference samples. The results show that high aspect ratio surface roughness at the nanometer scale significantly reduce the secondary emission yield of the surface. This reduction is more important for low electron energies, which is the most influencing energy range of electrons for multipactor. The multipactor region for the nanopillar coating

presenting the best secondary emission yield properties has been simulated, finding practical suppression of multipactor effect. The high-frequency surface resistance of these samples has also been estimated from published computations for similar surface roughness patterns. It was found that such nanopillar coatings are compatible with the best accomplishments of present space industry.

1. Introduction

Multipactor is an avalanche electron discharge (electron cloud) occurring in vacuum RF devices at high frequency and high power and in resonance with the RF field. It is initiated, fed, and sustained by secondary electron emission (SEE) from the device surfaces exposed to the electron discharge [1,2]. This electron discharge usually produces outgassing and eventually evolves into destructive Corona breakdown, a high intensity plasma [2]. These impairing phenomena affect severely the operation of communication, Earth observation, and other types of space satellites. It is also an important problem in high-energy particle accelerators, thermonuclear toroidal plasma fusion devices, klystron vacuum tubes for microwave generation, and other advanced equipment of great scientific, technological, industrial, economic, and social importance [3, 4, 5, 6]. Because of its relevance, suppression or mitigation of multipactor is being the objective of many leading and prestigious laboratories in the world during several decades (NASA, SLAC, CERN, KEK, ESTEC-ESA, VSC-ESA).

We have to note that, although multipactor in RF systems in space satellites and in vacuum accelerators share the same fundamental principles, the strategies for multipactor mitigation are different. As we will see below, high aspect ratio roughness surfaces are desired in space industry whereas this does not work for vacuum accelerators, as their main problem in these systems is the degasification produced by the electron cloud, thus the more

surface ratio the more possible degasification. In the following, all the material presented here refers to the first strategy.

Multipactor occurs when certain so-called resonance conditions are met among the RF field (frequency, intensity and geometry), the electron trajectories (initial emission and impact velocities and phases, distance between impacts) and the SEE properties of the surface material. Thus, the multipactor susceptibility results depend only on a frequency times gap (characteristic length) product and the RF field amplitude, apart from the material SEE properties. Of these, the SEE yield (SEY) for low impacting energies is the most influencing [7,8]. Because of the crucial role of SEE in multipactor, it is well established that the ultimate recourse against this phenomenon is the use of surfaces showing low SEY in critical parts of the RF device [5,6]. Therefore, research is focused on obtaining anti-multipactor coatings of very low SEY. In this sense, strategies based only on physicochemical properties of the surface materials have shown a limited capability because of surface *aging* on exposure to atmospheric air. On the other hand, recent results have demonstrated the significant dependence of SEE on surface roughness. High aspect ratio surface roughness at the micrometer scale leads to important reduction of the SEE, and thus to multipactor mitigation [7]. In fact, since the ESA workshop MULCOPIM 2005 [9] it is established that anti-multipactor coatings for space applications should be based on the SEE reduction by surfaces with high aspect ratio roughness [10,11,12,13,14]. Roughness reduces intrinsic (or flat mode) SEY by capturing part of the emitted electrons [15,16]. However, micrometric surface roughness of high aspect ratio present a new problem: the associated increase of RF surface resistance due to the skin effect of high-frequency electromagnetic waves [17,18], thus incrementing the RF power loss (insertion loss) of the device and limiting its efficiency. This drawback is becoming more demanding with the requirement of increasing frequency in space technology. Nevertheless, it can be solved by decreasing the depth of surface roughness while maintaining its high aspect ratio [10,12,13]. RF surface

resistance increases with both, aspect ratio and roughness depth. In particular, for ~10 GHz devices, the skin depth (penetration depth of the RF field) for Ag is ~ 630 nm, thus this implies that surface roughness depth in the nanometer scale makes negligible contribution to the RF surface resistance [17, 18]. Thus, a promising alternative is the creation at the surface of high aspect ratio nanometric structures.

Anti-multipactor coatings for space applications are particularly challenging mainly because they should be exposed to atmospheric air and they cannot afterward be *surface conditioned* in vacuum, as can be done in other applications. SEE aging in air increases SEY of most materials but it should be compensated for by surface roughness, however roughness of high size scale can affect to the macroscopic electromagnetic field of the device as well as to its RF surface resistance, which should be avoided. The research and progress in this specific applied domain has mainly been supported or published by ESA. As an indication of its youth and limited spread, the number of specific experimental contributions to MULCOPIM 2008 and 2017 were 4 and 8, respectively. This can roughly be estimated in more than 1/3 of worldwide contribution.

The main two required desiderata for anti-multipactor coatings in space industry has been quantified by recent research [7,12,13] as: a) low SEY: SEY maximum (σ_m) below 1.3, together with first cross-over energy (E_1) (SEY(E_1) = 1), higher than 200 eV; b) low RF surface resistance: below 1.4 times that of standard flat smooth Ag coating. Desideratum (a) implies strong surface roughness: high porosity (>50 %) and aspect ratio (>1.5) [19, 20]. On the other hand, condition (b) requires the surface material to be Ag in a thickness of more than 3 μm (for~10 GHz). In the case that thin overlayers are used for slowing down aging [7,14], requisite (b) also forces the surface capping overlayer to be much thinner than 50 nm. Finally, surface roughness depths of a few hundred nanometers size are also required to keep the RF surface resistance below the defined tolerance.

Anti-multipactor coatings used in space industry and even most in technological research do not achieve the above desideratum requirements (a) and (b). Thus, any practical approach to reach them is of huge interest. Having this in mind, in this work we explore the anti-multipactor capabilities of different coatings containing Ag nanopillars with high aspect ratio. We show that surfaces terminated in these nanopillars significantly reduce the secondary emission with respect to flat Ag coatings. Our approach is based on glancing angle deposition with DC magnetron sputtering [21]. With the appropriate choice of the deposition parameters, the momentum distribution and directionality of the sputtered species can be controlled. In the last few years it has been shown how glancing angle deposition with magnetron sputtering can produce nanopillar coatings of different metals [22,23,24]. The main advantage of this technique relies on its scalability, since sputtering is a physical technique in vacuum (thus with minimal recycling problems, since no aggressive waste is produced) able to coat large surfaces with relatively low energy consumption. The present research is original in its specific domain (anti-multipactor coatings for space applications) because of two main features: very high aspect ratio surface nanostructures and glancing angle magnetron sputtering deposition. Other features are: theoretical/simulation prediction of multipactor, theoretical/simulation estimation of RF behavior, and theoretical explanation of energy behavior of SEY reduction factor.

2. Materials and Methods

Two different kinds of samples have been fabricated by DC magnetron sputtering at RT in a UHV chamber (base pressure in the low 10^{-9} mbar range) onto 1 cm^2 Si substrates. Ag-terminated samples consist of a 2 nm thick adhesion layer of Ti, a continuous film of Ag (200 nm thick) and Ag nanopillars on top. On the other hand, Au-terminated samples consist of a 2 nm thick adhesion layer of Ti, a continuous film of Au (200 nm thick), Ag nanopillars and a final capping layer of Au, about 10 nm thick. Prior to the fabrication of these two

series, an initial set of samples without the continuous 200 nm Ag or Au thin film was fabricated in order to find the suitable conditions generating the desired morphologies. The fabricated and analyzed samples are summarized in Table I.

The sample stage is fully motorized, so that the substrate can be placed in front of the desired sputtering target and tilted when needed. The target diameter *d* is 5.1 cm for Ti and Ag and 3.8 cm for Au; and the distance between target and substrate *L* is 22 cm for Ti and 19 cm for Ag and Au. Argon is the sputtering gas and, in order to favor the ballistic regime (no collisions of the sputtered atoms with the plasma species and therefore high directionality), the pressure is the lowest allowing for stable plasma: 1.5×10^{-3} mbar. Moreover, cylindrical chimneys of 9 cm length and width of the same diameter as the target are placed on top of each magnetron source to increase the collimation of the sputtered material leading to the trapping of the thermalized sputtered species (i.e. those subjected to a high number of collisions, thus non-directional). The continuous thin films of Ti, Ag and Au have been deposited in the standard configuration, *i.e.* substrate parallel to the target. The power used for the deposition of thin films is 100, 60 and 20 W for Ti, Ag and Au, respectively. When a Au capping layer has been deposited, the substrate rotated ±25º in order to obtain a homogeneous coverage.

In order to fabricate the Ag nanopillars, we have used glancing angle deposition with 85º tilt angle between target and substrate. The length of the nanopillars is controlled by the deposition time. The obtaining of well-defined nanopillars is promoted by the high directionality of the atoms arriving at the substrate and their subsequent atomic shadowing effects related to the incidence at glancing angle. Although the deposition parameters favor the ballistic regime (the low gas pressure assures a low thermalization degree and the above mentioned chimney increases the collimation), atomic shadowing competes with the atoms mobility. In a first approximation, the adatom mobility depends inversely on the melting temperature T_m: the lower the T_m, the higher the mobility [25]. Thus, Ag (T_m=1235 K) has

higher adatom mobility than Au (T_m=1337 K) or Ti (T_m=1941 K), which makes more difficult obtaining nanostructured coatings made of silver. Lowering the temperature of the substrate would help, but the energy cost would prevent any application-oriented study. Our choice has been to rise the power, which increases the deposition rate and decreases the influence of mechanisms linked to surface mobility processes, since impinging new particles prevent the diffusion of the previous ones [26]. Thus, the Ag nanopillars have been fabricated with 300 W. Moreover, in order to minimize the incorporation of thermalized atoms, a particle collimator at the level of the substrate has been added to optimize the fabrication of the nanopillars [27, 28], see Fig.1(a). Other options proposed in the literature to increase the ratio of ballistic to thermalized atoms are the use of an area slit aperture [29] or the alignment between a segment of the racetrack on the target (i.e. the region with maximum ion impingement from the plasma) and the substrate when the L/d ratio is about 1.5 [30], but in our case L/d is almost 4. The particle collimator has the shape of a tunnel with 18 mm length and rectangular section (height: 4 mm, width: 14 mm), see Fig. 1(c), and it provides a good screen for thermalized atoms. By using the collimator, tilted nanopillars are obtained if the deposition takes place with the flux of sputtered atoms entering through one of the apertures of the tunnel. Vertical nanopillars have been also achieved by alternating deposition from both apertures [31]: depositing during 30 s from one side, rotating 180º the sample holder (the rotation axis being the normal to the substrate) and depositing again another 30 s from the other side; this process is repeated the desired number of times.

The morphology of the samples has been characterized by field emission scanning electron microscopy (FESEM), using a FEI Verios 460 high resolution electron microscope. The images were made at low voltage (2 kV) in order to get enough detail on the surface structure.

SEY measurements were performed using a Kimball Physics ELG-2 electron gun, which supplied the incident or primary electron beam: current ~3 nA, diameter ~2 mm, energy 20-2000 eV, fluence 0.5 μC/mm^2 per full energy scan. The electron gun current was previously calibrated with a Faraday cup and by measuring a graphite sample biased at +50 V. Additional information may be found elsewhere [7]. The SEY measurements were then performed by measuring the sample current to ground while sample was biased to -30 V with respect to the analysis chamber (VG Escalab 210 system at 3×10^{-9}mbar). Though SEY measurements were performed in a UHV analysis chamber, samples were previously exposed to atmospheric air for about 10 days except those of pure flat Ag or Au cleaned *in situ* in the analysis chamber by Ar ion bombardment. Standard samples of flat Ag or Au were exposed to atmospheric air for more than one month.

3. Results and Discussion

Fig. 1 shows FESEM images of representative samples with nanostructured Ag coatings fabricated with different parameters as well as a scheme of the deposition system. The sample shown in Fig. 1(b) was fabricated by simply tilting the substrate 85º with respect to the surface of the target, without using the particle collimator and with 40 min deposition time. The atomic flux during deposition was coming from the upper part of the sample and therefore, nanostructures tilted towards that direction are formed, although with a strong degree of coalescence, as it can be seen in the planar-view image. On the other hand, the sample in Fig. 1(d) (corresponding to sample #1163 from Table I) was made with the same deposition time but using the particle collimator shown in Fig. 1(c) in order to reduce the divergence of the arriving flux of atoms (the flux entered only from one aperture of the particle collimator). Comparing these two images, it is clear that the collimator successfully promotes the selective deposition of highly directed particles, thus favoring the atomic shadowing regime: as a result, well-defined nanopillars tilted towards the incoming flux are

formed. Only samples fabricated with the particle collimator, and thus with distinct nanopillars, have been analyzed regarding the SEY properties; they have been included in Table I.

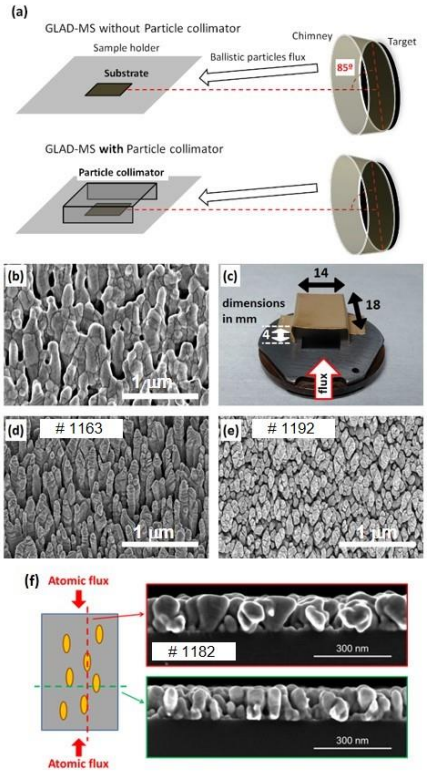

Fig. 1: (a) Scheme of the deposition system. (b) Example of sample fabricated without particle collimator. (c) Particle collimator, which has been offset to make visible the substrate below it. (d) Sample fabricated with the particle collimator and deposition from only one aperture (it corresponds to sample #1163 from Table I). (e) Sample fabricated with the particle collimator and alternative deposition from both apertures (sample #1192 from Table I). (f) Cross-sections along and perpendicular to the direction of the flux for a sample fabricated as that in panel (d), *i.e.*, with the particle collimator and alternative deposition from both apertures, but on Si (sample #1182 from Table I)

Finally, the sample shown in Fig. 1(e) (sample #1192 in Table I) was fabricated by alternative deposition from both apertures of the collimator (30 s deposition time in each position and 40 repetitions), corresponding to the top and bottom sides of the image. As it can be seen in the planar-view, vertical nanopillars oriented along that axis have been formed. To get a more detailed insight on the geometry of the vertical nanopillars, an equivalent sample has been fabricated directly on Si substrate (without the continuous film). Its cross-section FESEM images are shown in Fig. 1(f). The cross-section images confirm

that the nanopillars are elongated in the direction of the atomic flux. This sample corresponds to sample #1182 in Table I.

The shape of the nanopillars has been deduced from SEM measurements: top-view inspection of all samples and cross-sections of selected ones, namely #1182, #1184 and #1192. Although the sputtering rate is constant, due to the atomic shadowing mechanism and the use of the particle collimator, the nanopillars grow with the shape of inverted truncated cones with ellipsoidal cross-section. As the nanopillars become wider as they grow, the growth rate in the vertical direction decreases with time. Thus, the average length of the nanopillars is 150 nm for sample #1184 (13 min deposition time) and 300 nm for sample #1192 (40 min), and it is estimated to be about 470 nm for samples #1219, #1220, #1229 and #1230 (70 min).

The lateral dimensions of the nanopillars and the spacing among neighboring pillars also depend on the deposition time, as the nanopillars become wider as they grow. Some representative values are:

-Sample #1192, vertical pillars with ellipsoidal top base with 300 nm ± 75 nm long axis and 100 nm ± 25 nm short axis, spacing between 10 and 40 nm. Fig. 2 (a) shows representative SEM images of this sample, not only top-view but also cross-sections along two perpendicular directions.

-Sample #1219, vertical pillars with ellipsoidal top base with 1100 nm ± 300 nm long axis and 390 nm ± 90 nm short axis, spacing between 50 and 100 nm. Fig. 2 (b) shows top-view of this sample as well as that of #1220, whose SEM properties will be compared below.

- Sample #1163, tilted pillars with diameter 75 nm ± 30nm; spacing is bigger in tilted nanopillars compared to vertical ones, here is from 50 to 150 nm.

It is also worth noting that SEM images of Au-terminated samples obtained with back-scattered electron do not show inhomogeneities, which is an indication of a rather uniform coating.

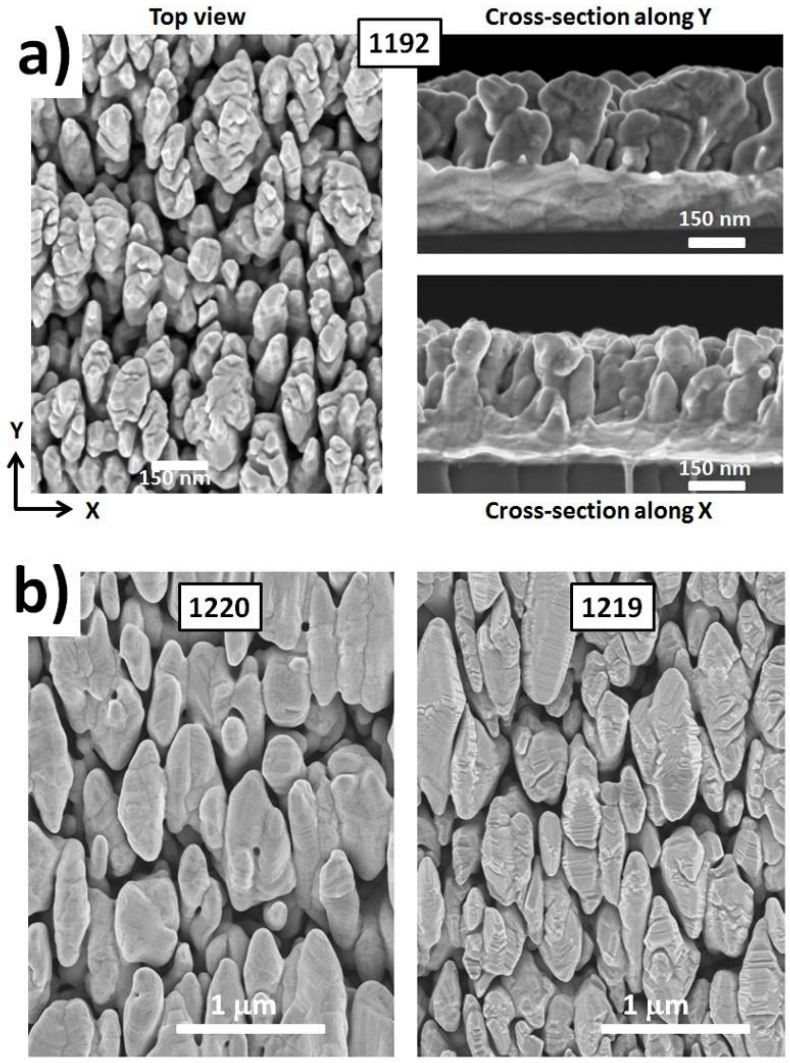

Fig.2: a) SEM images of sample #1192, top-view (left panel) and cross-sections along two perpendicular directions; x (bottom) and y (top). b) Top view SEM images of Ag nanopillars grown on Ag (sample #1220) and on Au (sample #1219).

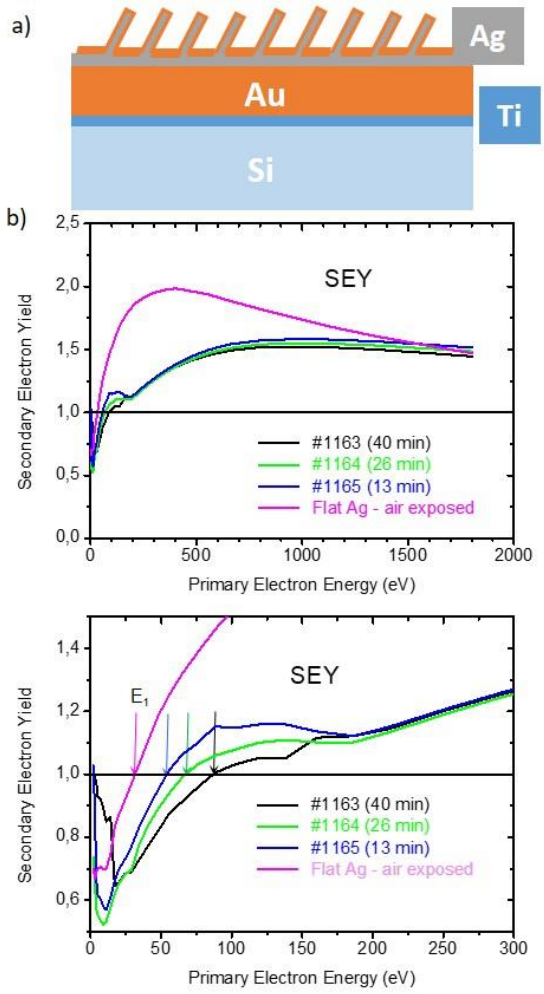

Fig.3: a) Scheme of the Au-terminated samples; b) SEY-energy curves of Au-terminated samples with tilted Ag nanopillars fabricated with 13, 26 and 40 min deposition time (samples #1165, #1164 and #1163 in Table I). c) Low energy region of the above curves. Pink curve corresponds to a flat smooth sample of standard Ag plating from space industry exposed to the air (sample Ag Ref. in Table I).

Fig.3 shows the SEY-energy curves of three Au-terminated samples with tilted Ag nanopillars fabricated with 13, 26 and 40 min deposition time (samples #1165, #1164 and #1163 from Table I). Longer deposition time leads to longer pillars, thus to higher aspect ratio nanostructures. The curve of a flat smooth sample of a standard Ag plated piece from space industry exposed to air for several weeks is also included in Fig. 3 as a reference. The nanopillar coatings offer an improved SEE behavior compared to the reference Ag surface.

It is worth noting that the first cross-over energy E_1 (indicated by arrows for each sample) increases and the maximum value of the SEY (σ_m) decreases with deposition time. Sometimes, the parameter E_1/σ_m has been used as *Figure of Merit* (*FoM*) since multipactor threshold was often found to be approximately proportional to $(E_1/\sigma_m)^s$ for some *s* about 0.7 [7], which reveals the increased influence of SEY at low energies on multipactor. As it can be seen from Fig. 3 and Table I, the nanopillar surfaces with higher aspect ratio exhibit higher *FoM*.

SAMPLE	**substrate**	**nanopillars**			**SEY**				
		angle	deposition time (min)	capping	E_1 (eV)	σ_m	E_m (eV)	σ_{1800}	*FoM* (eV)
#1109	Si	t,coal.	90	-	37	1,63	538	1,34	23
#1108	Si	t	90	-	29	2,06	430	1,57	14
#1165	Au(200)/Ti/Si	t	13	Au	54	1,58	1013	1,52	34
#1164	Au(200)/Ti/Si	t	26	Au	68	1,55	1007	1,49	44
#1163	Au(200)/Ti/Si	t	40	Au	88	1,52	960	1,44	58
#1182	Ti/Si	v	13	-	65	1,43	720	1,24	45
#1184	Au(200)/Ti/Si	v	13	Au	21	1,40	1074	1,38	15
#1192	Au(200)/Ti/Si	v	40	Au	46	1,31	1045	1,29	35
#1219	Au(200)/Ti/Si	v	70	Au	153	1,47	1034	1,41	104
#1220	Ag(200)/Ti/Si	v	70	-	169	1,37	788	1,26	123
#1230	Polished Ag	v	70	Au	79	1,28	926	1,24	61
#1229	Polished Ag	v	70	-	132	1,25	711	1,17	106
Ag Ref.	Ag	-			31	1,98	391	1,47	16
Au Ref.	Au	-			26	1,98	575	1,64	13

Table I. Analyzed samples and their SEY parameters. The basic sample structure is defined by capping/nanopillars/substrate. The table collects the presence or absence of each of these components. The capping thickness is around 10 nm. The nanopillars geometry is described as: t-tilted; v-vertical, coal- highly coalesced nanopillars. The deposition rate of the nanopillars is around 10 nm/min, with some deviations associated to the placement of the particle collimator and to the deposition-taking place from only one or both apertures. A Ti layer within the substrate refers to a 2 nm thick adhesion Ti layer. The Au (200) or Ag (200)

layers refer to 200 nm thick continuous films. Polished Ag are substrates made from Ag and subsequently polished. The samples Ag Ref. and Au Ref. correspond to standard industry flat smooth samples.

Table I collects the main SEY parameters of all samples studied here, including the Ag and Au reference samples with industry standard flat smooth surfaces. The best results in terms of *FoM* were obtained with vertical nanopillars, i.e. fabricated by alternative deposition from opposed sides of the particle collimator. Regarding the error of the σ parameter from SEY measurements, it has been stablished that $|\Delta\sigma| < 0.05$ [32].

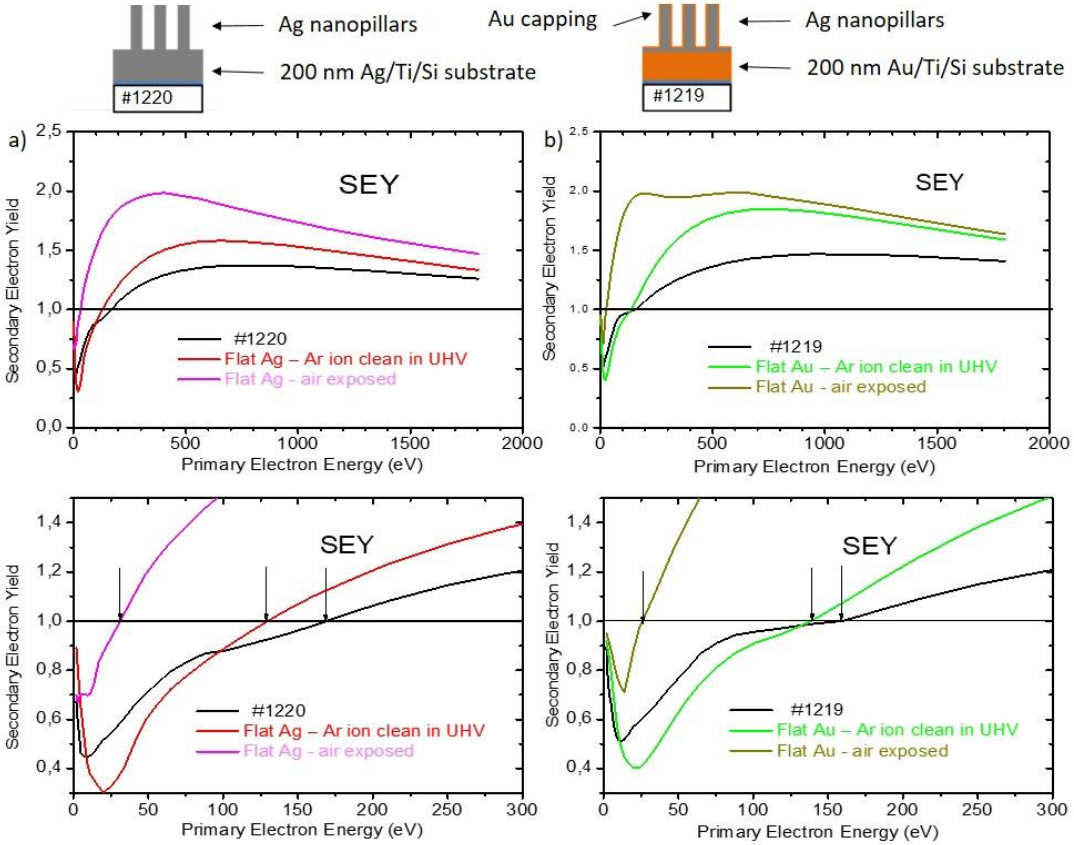

Fig. 4: a) SEY-energy curve of a Ag-terminated sample with vertical Ag nanopillars (sample #1220) compared to those of a flat smooth sample of standard Ag plating from space industry exposed to the air and the same reference Ag plating after cleaning with Ar ion bombardment in UHV; b) SEY-energy curve of an Au-terminated sample with vertical Ag nanopillars (sample #1219) compared to those of a flat smooth air exposed Au sample and the same surface after clean preparation in UHV. The inferior panels show the low energy regions in more detail.

Indeed, the best samples (numbers #1219, #1220 and #1229) were made of vertical nanopillars of about 470 nm height and 1100x390 nm2 lateral average dimensions (see Fig. 2(b)) with about 60 % of surface coverage, grown on top of Ag or Au. Fig. 4 shows the SEY plots corresponding to these samples: Fig. 4 (a) contains that of the Ag-terminated nanopillars grown on a 200 nm thin film of Ag (sample #1220) and Fig. 4 (b) that of the Au-terminated terminated nanopillars grown on a 200 nm thin film of Au (sample #1219). Since these nanopillars are covered with a Au capping layer, the incident electrons impinge on a fully Au covered sample. The 200 nm thick Au substrate is intended to avoid possible deficient coverage of the Au capping layer between nanopillars. We will first discuss the case of the simplest structure, i.e. the Ag-terminated nanopillars, as it consists of an all-Ag sample. Fig. 4 (a) shows the SEY-energy curve of this sample compared with those of a flat smooth pure Ag sample cleaned by Ar ion bombardment in UHV and of a similar flat smooth Ag surface after exposure to the air for several weeks. This last SEY-energy curve corresponds to a standard Ag plated piece from space industry. SEY curves of homogeneous materials with a flat surface are expected to be simple and unimodal, convex with one maximum at low energies followed by one inflection point and therefore becoming concave at higher energies. Any additional structure has always been explained by lateral (patches) or in depth (layers) inhomogeneities. Taking the SEY response of the UHV clean Ag surface as the reference for homogeneous smooth Ag, we can see that its exposure to air induces a strong peak or shoulder at energies below 600 eV due to surface contamination. A small shoulder at low energies is also present for the nanopillar sample, which would be assigned to some surface contamination from air exposure if it would correspond to a flat smooth sample (nanopillar samples were too exposed to the air). There is no theoretical or experimental evidence, in any case very scarce, for surface roughness alone to produce such a shoulder. A similar shoulder has been found in tilted nanopillars (see Fig. 3).

In Fig. 4 (b), we present the SEY-energy curve of the Ag nanopillars with Au capping (sample #1219) along with those of a flat smooth Au sample cleaned in UHV and after air exposure. It should be clarified here that, since the electron range in Au exceeds 10 nm for energies higher than about 800 eV [33], the sample made of Ag nanopillars with 10 nm Au capping cannot be considered as being all-Au from the point of view of SEY at those energies. In the case of the flat smooth Au exposed to air, again a shoulder at low energies appears. This shoulder is clearly distinct here because it is less intense than that appearing for Ag and more separated from the maximum due to the contribution of the bulk. In the case of Au, this shoulder is again attributed to the presence of a thin surface layer coming from adsorption. The energy, the intensity, and the width of the peak related to the surface layer increase with its thickness [34] and may become blurred with the bulk contribution as in the case of Ag where both, adsorption and absorption, participate. The presence of the shoulder can also be observed for the capped nanopillars (also exposed to the air).

Other nanopillar samples showed lower values of E_1 or higher values of σ_m, as displayed in Table I. Some samples showed an evident shoulder at low energies affecting visibly the value of E_1. It should be noticed that the presence of a shoulder was associated to low values of σ_m and $\sigma_m/\sigma(E>>E_m)$ and high values of E_m (energy value for σ_m). These two last characteristics are typical of the modification of SEY by surface roughness of high aspect ratio.

The relative SEY curves for the same nanopillar sample shown in Fig. 4 are shown in Fig. 5. Relative SEY is defined as the ratio of the SEY curve corresponding to the nanopillar surface (exposed to the air) to the curve of smooth flat surfaces of the corresponding pure metal (Ag or Au) exposed to air. In this way, we obtain a SEY reduction factor related only to the surface morphology. The first thing to observe from Fig. 5 is that this hypothetical SEY topographical reduction factor thus defined is dependent on the energy of primary electrons. In fact, its energy dependence qualitatively resembles that of the backscattered

electron emission yield, η [35,36]. At very low energies, η shows an abrupt decrease due to elastically backscattered primary electrons and then a gradual increase due to inelastically backscattered ones. Actually, that is the origin of the observed dependency for the relative SEY: backscattered electrons are more relevant for the SEY of rough surfaces. The relative SEY is in some way related to the ratio of backscattered to true secondary electron emission. While many true secondary electrons are intercepted and absorbed by the roughness due to their very low energies, intercepted backscattered produce further second-generation secondary electron emission. We may approximately summarize the argument:

$$Relative\ SEY = \frac{\sigma_{rough}}{\sigma_{flat}} = \frac{R \cdot \delta + R' \cdot \eta + \delta^{(2)} + \eta^{(2)}}{\delta + \eta} \approx R + \frac{\delta^{(2)}(\eta)}{\delta}$$

where $SEY = \sigma = \delta + \eta$, being δ the true secondary and η the backscattered electrons emission yields, with $\delta >> \eta$; R is the proper topographical reduction factor (because the emission angle distribution of true secondary electrons or cosine law of Lambert is independent of material and of primary energy); R' corresponds to the reduction factor for backscattered electrons, with $R' \approx R$ but somehow dependent on material and primary energy; and $\delta^{(2)}$, $\eta^{(2)}$ are the second and higher order emission produced by backscattered electrons intercepted by the surface roughness, $\delta^{(2)} >> \eta^{(2)}$. By writing $\delta^{(2)}(\eta)$, we stress the fact that those secondary electrons are produced by intercepted backscattered electrons and thus approximately proportional to η. Above arguments and equation are a very rough approximation (first order) which predicts the general energy trend of relative SEY of rough surfaces of most materials. η is neglected against δ because $\delta \approx 1.45 \pm 0.25$ and $\eta \approx 0.30 \pm 0.15$. R is the solid angle integral of the Lambert emission probability ($\propto \cos(\theta)$, θ = polar angle = emission angle) [35, 36] over the solid angle free of surface roughness interference, thus a pure geometrical quantity. Since for backscattered electrons, the Lambert law is not exactly fulfilled and the difference is slightly dependent on energy and on material [35, 36],

R' is only slightly different from R, and $R'\cdot\eta$ is neglected against $R\cdot\delta$. The equation relays also on the fact that secondary electrons, with low energies, are not able to produce significant 2nd order emission, and thus $\sigma^{(2)}(\delta+\eta) \approx \sigma^{(2)}(\eta) \approx \delta^{(2)}(\eta)$. The general qualitative shape of graphs in Fig.4 has already been found in other cases [37].

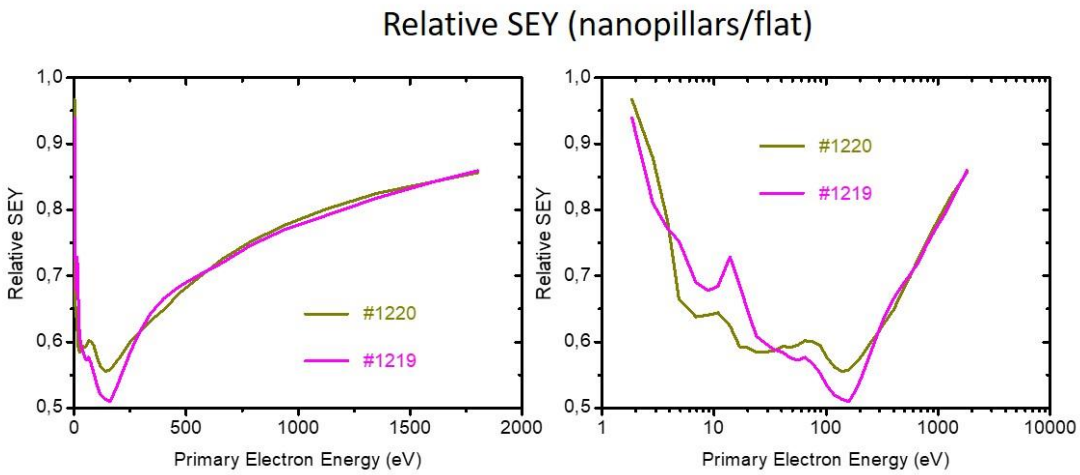

Fig. 5: a) Relative SEY curves for samples #1220 and #1219. The relative SEY curves are obtained by dividing the SEY curve of those samples with that of the flat smooth samples of Ag and Au exposed to the air, respectively. b) Relative SEY for the same samples in semi-logarithmic scale.

Fig. 5 also shows an apparent independence of the relative SEY on the material. That is not expected since the relative SEY should depend on the material SEE properties, see equation above. This coincidence is possibly due to a very similar ratio of backscattered to true secondary electron emission in Ag and Au. The small structure at about 70 eV in both relative SEY curves is due to the shoulder appearing in the SEY curves of both nanopillar samples, see Fig.4 (a) and (b). That shoulder could reasonably be ascribed to surface contamination from air exposure, as discussed above. This is supported by the fact that it appears with different relative intensities in different samples. The question is why they are not so clearly distinguished in the flat smooth samples so that they would be canceled by

offsetting in the relative SEY curves. An explanation could be that the contamination surface layer in the nanostructured surfaces is much thinner and consequently we were not using the adequate flat smooth surface as SEY reference. Another plausible explanation could be that those structures belong to the backscattered electrons emission yield-primary energy curves, which are enhanced in the relative SEY ones. A similar structure appears at 60 eV in new theoretical calculations of the backscattered emission [38].

As assessment of the experimental SEY results, we have made an estimation of the possible multipactor power-threshold improvement with these nanopillar coatings. We have used a multipactor simulation software tool, MEST [36], which has been proved in similar applications. Fig.6 shows the multipactor regions for an infinite parallel plate geometry (applicable locally to many RF devices) with SEY properties either as those of sample #1220 (blue line) or of the flat smooth Ag reference sample (red line). The multipactor regions correspond to those enclosed by the lines. In the interval of most interest, 10-40

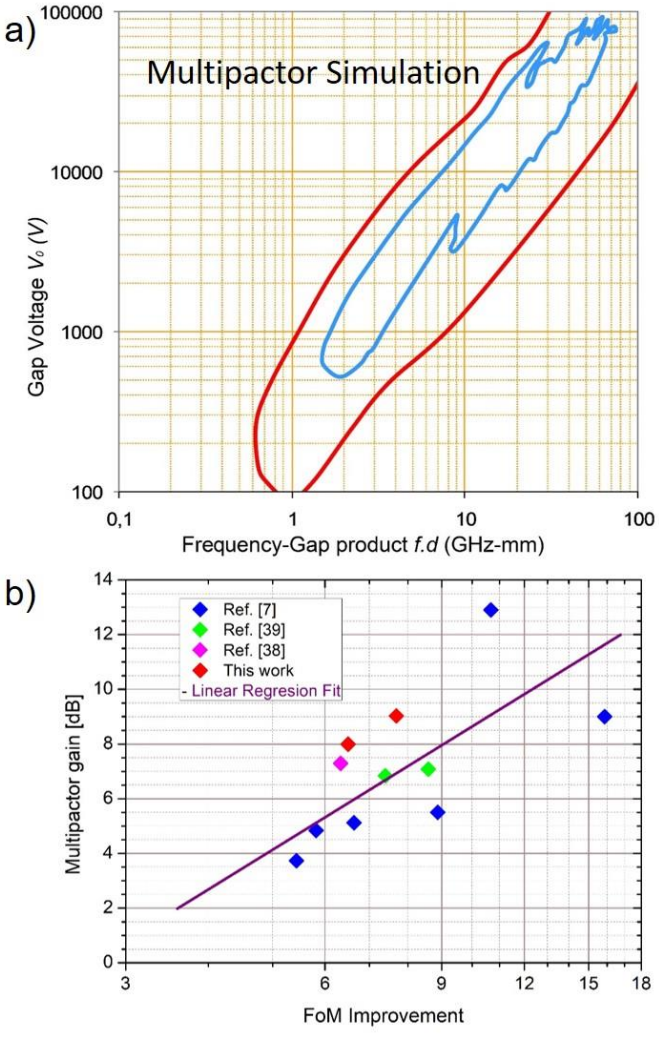

GHz-mm, the multipactor power-threshold improvement (with respect to the standard Ag plating) is

Fig. 6: (a) Simulation of the multipactor region thresholds with MEST software [35] for infinite parallel geometry and SEY properties of the surface of sample #1220 (blue) and flat smooth Ag plating exposed to the air (red) sample. RF power is proportional to gap voltage squared. (b) Experimental correlation among SEY and Multipactor for various technological prototypes including hypothetical ones with nanopillar coatings of this work. Red symbols, this work; blue symbols, Ref. [7]; violet symbols, Ref. [39]; and green symbols, Ref. [40]. See text.

computed by MEST as 9.0 dB. This power increase is over the limit of most multipactor test beds [7, 10, 12], and it means practical suppression of multipactor.

The other important property of anti-multipactor coatings is its RF surface resistance. The requirement of less than 1.4 times that of standard Ag plating is very demanding. It is even difficult to measure it with a resonant cavity, and it is better tested by the insertion loss of specially designed waveguides [10, 12]. In this line, a rough estimation has been made for sample #1220 using the results of calculations for different regular patterns of surface roughness [17,18]. One problem is found: our nanopillar coatings do not show those highly regular patterns and they present higher aspect ratios. We propose therefore the RF surface resistance value of rectangular transverse grooves as an upper bound for our case. The groove parameters were taken as those of the average nanopillar pattern, and they have been obtained by several strong approximations. First, a regular centered rectangular pattern of cylindrical nanopillars of elliptical section was calculated with the same average coverage, about 50%, and the same average periods, 660 and 1250 nm, for the two directions transversal and parallel to deposition flux, respectively (transversal grooves should show higher RF surface resistance). Then, a rectangular groove pattern with a period four times the skin depth (320 nm for Ag at 40 GHz) and height equal to half the period was assumed

for the higher RF surface resistance compatible with the nanopillar parameters according to results of Matsushima and Nakata [18]. These show a value of 1.5 times that of the flat smooth surface. This is thus a very conservative upper bound. In conclusion, it is expected that our nanopillar coatings would not significantly deteriorate device RF insertion loss.

Finally, we present in Fig.6 (b) a comparison with other technological proposals for anti-multipactor coatings for which we have sufficient experimental information about both, SEY properties (particularly, *FoM*) and multipactor power threshold (*MPT*) of application waveguides. For the coatings #1219 and #1220 of this work, we have used theoretical multipactor power threshold values from simulation with MEST.

As mentioned above (see also Ref. [7]) some correlation is expected between both experimental parameters. In order to compare waveguides of different geometrical structures working at different frequencies and with different RF power scales, it is necessary to use relative values. In Fig.6 (b), we have used present standard technology, i.e., standard (smooth and flat) silver plating as the reference. Thus, *FoM improvement* is *FoM*(coating)/*FoM*(Ag plating) and *MPT gain* is 10×log(*MPT improvement*) where *MPT improvement* is *MPT*(device with coating)/ *MPT*(device with Ag plating). The linear correlation shown is

$$MPT\_improvement = \frac{MPT}{MPT_{ref}} = G \cdot \left(\frac{FoM}{FoM_{ref}} \right)^{1.5} = G \cdot \left(FoM\_improvement \right)^{1.5}$$

where $G = 0.23$.

We can observe that SEY properties and multipactor performance of the nanopillar coatings are both very good. *MPT gain* values higher than 8 are difficult to measure and represent practical multipactor suppression. The MEST estimated values for nanopillar coatings are probably somehow high because *MPT* testing usually implies some manipulation and SEY deterioration. However, they are still inside error of Fig.6, about 2 dB.

Other important properties of coatings in Fig.6 (b) were the following ones: Ref. [40] coatings were of protuberances in the 100 nm size scale (similar to the nanopillar ones) and with device insertion loss also bellow 1.5 times that of standard Ag plating; Ref. [7] coatings were of protuberances in the 1 μm size scale and with device insertion loss about 2.6 times that of standard Ag plating; Ref. [39] coatings were of pores in the 1 μm size scale and with device insertion loss about 2.2 times that of standard Ag plating.

4. Summary and conclusions

Relatively simple and practical experimental setup and corresponding procedure have been used for preparing coatings of Ag nanopillars by glancing angle magnetron sputtering deposition. Nanopillars were either vertical (normal to the substrate) or tilted, with dimensions well below the micron scale, high aspect ratio, and high surface density or coverage. These are known characteristics for reducing secondary electron emission and consequently for providing good anti-multipactor coatings. Secondary electron emission yield was measured and found to be reduced with respect to flat samples by a factor depending on primary electron energy, this reduction being more pronounced for low energies. This energy dependence could be explained by the contribution of second order secondary electrons to the SEY of rough surfaces (*i.e.* secondary electrons produced by first order backscattered electrons acting as primary ones on surface protuberances).

It was also found that the SEY reduction increased with the aspect ratio of nanopillars. The reduction for the higher aspect ratio values was found to be sufficient for practical suppression of multipactor by means of a numerical simulation tool (MEST). It was also estimated, by comparison with published simulation results, that the submicron size scale of the surface roughness depth maintained high-frequency RF surface resistance quite below the industry requirements. Glancing angle magnetron sputtering deposition thus

appears to be a practical technique for producing anti-multipactor coatings for application in space industry.

Acknowledgments This investigation has been funded by the MINECO of Spain through the AYA2012-39832-C02-02, FIS2015-67367-C2-1-P, MAT2015-69035-REDC and MAT2014-59772-C2-1-P projects and by the Comunidad de Madrid through the NANOMAGCOST-CM Ref: P2018/NMT4321 project. One of the authors (C.M.) thanks MECD for FPU14/02020 grant. The authors also want to thank SEGAINVEX and SIdI from UAM for technical support, and to acknowledge the service from the MiNa Laboratory at IMN funded by Comunidad de Madrid (S2018/NMT-4291 TEC2SPACE), MINECO (CSIC13-4E-1794) and the European Union (FEDER, FSE).

References:

[1] Rami A. Kishek, Y.Y. Lau, L.K. Ang, A. Valfells, and R.M. Gilgenbach: Multipactor discharge on metals and dielectrics: Historical review and recent theories, Phys. Plasmas 5(1998) 2120–2126. https://doi.org/10.1063/1.872883.

[2] G.-Y. Sun, B.-P. Song, B.-H. Guo, R.-D. Zhou, S. Zhang, H.-B. Mu and G.-J. Zhang, Estimation of surface flashover threshold in vacuum: from multipactor to discharge plasma, J. Phys. D: Appl. Phys. 51(2018)295201. https://doi.org/10.1088/1361-6463/aacccf.

[3] European Cooperation for Space Standardization (ECSS), Space engineering: Multipaction design and test, ECSS-E-20-01A Rev.1, 1 March 2013. http://everyspec.com/ESA/download.php?spec=ECSS-E-20-01A_REV-1.047803.pdf.

[4] R. G. Carter in “Microwave and RF Vacuum Electronic Power Sources”. Cambridge University Press, Cambridge 2018. https://doi.org/10.1017/9780511979231.

[5] M. A. Furman, Electron cloud effects in accelerators, CERN Yellow Report CERN-2013-002 (2013) 1–8, arXiv:1310.1706v1 [physics.acc-ph]. https://arxiv.org/abs/1310.1706.

[6] J. Hillairet, M. Goniche, N. Fil, M. Belhaj, J. Puech, Multipactor in High Power Radio-Frequency Systems for Nuclear Fusion, MULCOPIM (Multipactor, Corona and Passive Intermodulation) (Apr 2017) Noordwijk, Netherlands, arXiv:1710.03629 [physics.plasm-ph]. https://arxiv.org/abs/1710.03629.

[7] V. Nistor, L. A. González, L. Aguilera, I. Montero, L. Galán, U. Wochner, D. Raboso, Multipactor suppression by micro-structured gold/silver coatings for space applications, Appl. Surf. Sci. 315 (2014) 445–453.https://doi.org/10.1016/j.apsusc.2014.05.049

[8] N. Fil, M. Belhaj, J. Hillairet, J. Puech. Multipactor threshold sensitivity to total electron emission yield in parallel-plate waveguide and TEEY models accuracy. Phys. Plasmas 23 (2016)123118. https://doi.org/10.1063/1.4972571.

[9] D. Wolk, P. Lozano, M. García, I. Montero, L. Galán, C. Prieto, F. Galán-Estella, E. García-Camarero, D. Raboso, Coatings on Mg alloys for reduction of Multipactor effects in RF components, in: 5th International Workshop on Multipactor, Corona and Passive Intermodulation in Space RF Hardware, MULCOPIM 2005, European Space Agency (2005).

[10] V. C. Nistor, L. Aguilera, I. Montero, D. Raboso, L. A. González, L. Soriano, L. Galán, U. Wochner, D. Wolk, Strategies for Anti-Multipactor Coatings of Suppressed Secondary Emission and Low Insertion Losses for High Power RF Components in Satellite Systems, in: 7th International Workshop on Multipactor, Corona and Passive Intermodulation in Space RF Hardware, MULCOPIM 2011, European Space Agency (2011).

[11] L. Aguilera, I. Montero, M. E. Dávila, A. Ruiz, L. Galán, V. Nistor, D. Raboso, J. Palomares, F. Soria, CuO nanowires for inhibiting secondary electron emission. J. Phys. D: Appl. Phys. 46 (2013) 165104. https://doi.org/10.1088/0022-3727/46/16/165104.

[12] V. C. Nistor, L. A. González, L. Aguilera, I. Montero, L. Galán, U. Wochner, D. Raboso,L. Soriano, Nanostructured Au/Ag anti-multipactor coatings with RF surface conductivity as standard silver plating, in: 8th International Workshop on Multipactor, Corona and Passive Intermodulation in Space RF Hardware, MULCOPIM 2014, European Space Agency (2014).

[13] L. Soriano, G. Troncoso, A. Gudín, C. Morales, V. Nistor, J. A. González, L. Galán, Preliminary results of research on new rough Ag anti-multipactor coatings with no insertion loss and aging drawbacks, in: 9th International Workshop on Multipactor, Corona and Passive Intermodulation in Space RF Hardware, MULCOPIM 2017, European Space Agency (2017).

[14] D. D. Wu, J. Z. Ma, Y. Bao, W. Z. Cui, T. C. Hu, J. Yang, Y. R. Bai, Fabrication of Porous Ag/TiO_2/Au Coatings with Excellent Multipactor Suppression, Sci. Rep. 7 (2017) 43749.https://doi.org/10.1038/srep43749.

[15] M. Pivi, F. K. King, R. E. Kirby, T. O. Raubenheimer, G. Stupakov, F. Le Pimpec, Sharp reduction of the secondary electron emission yield from grooved surfaces, J. Appl. Phys. 104 (2008) 104904.https://doi.org/10.1063/1.3021149.

[16] D. Wang, Y.N. He, M. Ye, W.B. Peng, W.Z. Cui, Secondary electron emission characteristics of nanostructured silver surfaces, J. Appl. Phys. 122 (2017) 153302.https://doi.org/10.1063/1.4989965.

[17] M. V. Lukic and D. S. Filipovic, Modeling of 3-d surface roughness effects with application to μ-coaxial lines, IEEE Trans. Microw. Theory Tech. 55 (2007) 518–525.https://doi.org/10.1109/TMTT.2007.891688.

[18] A. Matsushima and K. Nakata, Power loss and local surface impedance associated with conducting rough interfaces, Elect. Commun. Jpn. 89 (2006) 1–10. https://doi.org/10.1002/ecjb.20218.

[19] M. Ye, Y. N. He, S. G. Hu, R. Wang, T. C. Hu, J. Yang, and W. Z. Cui, Suppression of secondary electron yield by micro-porous array structure, J. Appl. Phys. 113 (2013) 074904. https://doi.org/10.1063/1.4792514.

[20] W-Z. Cui, Y. Li, J. Yang, T-C. Hu, X-B. Wang, R. Wang, N. Zhang, H-T. Zhang, Y-N. He, An efficient multipaction suppression method in microwave components for space application. Chinese Phys. B 25 (2016) 068401. https://doi.org/10.1088/1674-1056/25/6/068401.

[21] J. C. Sit, D. Vick, K. Robbie, M. J. Brett, Thin Film Microstructure Control Using Glancing Angle Deposition by Sputtering, J. Mater. Res. 14 (1999) 1197–1199. https://doi.org/10.1557/JMR.1999.0162.

[22] P.Pedrosa, A. Ferreira, J.M. Cote, N. Martin, M. Arab Pour Yazdi, A. Billard, S. Lanceros-Mendez, F. Vaz, Influence of the sputtering pressure on the morphological features and electrical resistivity anisotropy of nanostructured titanium films, Appl. Surf. Sci. 420(2017)681–690. http://dx.doi.org/10.1016/j.apsusc.2017.05.175.

[23] R. Álvarez, J. M. García-Martin, A. García-Valenzuela, M. Macías-Montero, F. J. Ferrer, J. Santiso, V. Rico, J. Cotrino, A. R. Gonzalez-Elipe, A. Palmero, Nanostructured Ti thin films by magnetron sputtering at oblique angles, J. Phys. D: Appl. Phys. 49 (2016) 045303. https://doi.org/10.1088/0022-3727/49/4/045303.

[24] J. Dervaux, P. A. Cormier, P. Moskovkin, O. Douheret, S. Konstantinidis, R. Lazzaroni, S. Lucas, R. Snyders, Synthesis of nanostructured Ti thin films by combining glancing angle deposition and magnetron sputtering: A joint experimental and modeling study, Thin Solid Films 636 (2017) 644– 657. http://dx.doi.org/10.1016/j.tsf.2017.06.006.

[25] D. P. Singh, P. Goel, J. P. Singh, Revisiting the structure zone model for sculptured silver thin films deposited at low substrate temperatures, J. Appl. Phys. 112 (2012) 104324. https://doi.org/10.1063/1.4767634.

[26] R. Alvarez, J. M. García-Martín, M. Macías-Montero, L. González-García, J. C. González, V. Rico, J. Perlich, J. Cotrino, A. R. González-Elipe, A. Palmero, Growth regimes of porous gold thin films deposited by magnetron sputtering at oblique incidence: from compact to columnar microstructures, Nanotechnology 24 (2013) 045604. https://doi.org/10.1088/0957-4484/24/4/045604.

[27] A. García-Valenzuela, R. Alvarez, V. Rico, J. Cotrino, A.R. González-Elipe, A. Palmero, Growth of nanopillar porous TiO_2 thin films by magnetron sputtering using particle collimators, Surf. Coat. Technol. 343 (2018) 172–177. http://doi.org/10.1016/j.surfcoat.2017.09.039.

[28] S. Maidul Haque, K. Divakar Rao, S. Tripathi, R. De, D.D. Shinde, J.S. Misal, C. Prathap,M. Kumar, T. Som, U. Deshpande, N.K. Sahoo, Glancing angle deposition of SiO_2 thin films using a novel collimated magnetron sputtering technique, Surf. Coat. Technol, 319 (2017)61– 69. http://dx.doi.org/10.1016/j.surfcoat.2017.03.056.

[29] C. Khare, C. Patzig, J. W. Gerlach, B. Rauschenbach, B. Fuhrmann, Influence of substrate temperature on glancing angle deposited Ag nanorods, J. Vac. Sci. Technol. A 28 (2010) 1002. https://doi.org/10.1116/1.3447231.

[30] A.-A. El Mel, N.Stephant, J.Hamon, D.Thiry, A. Chauvin, M. Chettab, E. Gautron, S. Konstantinidis, A. Granier, P.-Y.Tessier, Creating nanoporosity in silver nanocolumns by direct exposure to radio-frequency air plasma, Nanoscale 8 (2016) 141–148. https://doi.org/10.1039/C5NR07145C.

[31] K. M. Krause, M. T. Taschuk, M. J. Brett, Glancing angle deposition on a roll: Towards high-throughput nanostructured thin films, J. Vac. Sci. Technol. A 31 (2013) 031507.https://doi.org/10.1116/1.4798947.

[32] P. Mader et al., "TAS-F multipactor results in EVEREST project," The 8th European Conference on Antennas and Propagation (EuCAP 2014), The Hague, 2014, pp. 1651-1654. DOI: 10.1109/EuCAP.2014.6902104.

[33] W. S. M. Werner, Electron transport in solids, in: D. Briggs and J. T. Grant (Eds.), Surface Analysis by Auger and X-ray Photoelectron Spectroscopy, IM Publications Chichester, UK, 2003.

[34] S. Yu, W. Yi, T. Jeong, J. Lee, J. Heo, C. S. Lee, D. Jeon, J. M. Kim, Secondary electron emission for layered structures, J. Vac. Sci. Technol. A 20 (2002) 950–952.https://doi.org/10.1116/1.1472415.

[35] M. A. Furman and M. T. F. Pivi, Probabilistic model for the simulation of secondary electron emission, Phys.Rev. ST Accel. Beams 5 (2002) 124404. https://doi.org/10.1103/PhysRevSTAB.5.124404.

[36] J. de Lara, F. Pérez, M. Alfonseca, L. Galán, I. Montero, E. Román, D. Raboso, Multipactor prediction for on-board spacecraft RF equipment with the MEST software tool, IEEE Trans. Plasma Sci. 34 (2006) 476–484.https://doi.org/10.1109/TPS.2006.872450.

[37] D. Wang, Y.N. He, M. Ye, W.B. Peng, W.Z. Cui, Secondary electron emission characteristics of nanostructured silver surfaces, J. Appl. Phys. 122(2017) 153302. https://doi.org/10.1063/1.4989965.

[38] J. Pierron, C. Inguimbert, M. Belhaj, T. Gineste, J Puech, M. Raine, Electron emission yield for low energy electrons: Monte Carlo simulation and experimental comparison for Al, Ag, and Si, J. Appl. Phys. 121 (2017) 215107. https://doi.org/10.1063/1.4984761.

[39] D. Wolf, I. Montero, L. Galan and D. Raboso: Method and structure for inhibiting multipactor. US patent. 13-09-2006, Atty Dkt: F-9209, spec v7 {PC20}.wpd. Tesat spacecom, ICMM-CSIC, UAM and ESA, (2006).

[40] V. C. Nistor: New approaches to anti-multipactor coatings for space applications. Doctoral Thesis. Universidad Autónoma de Madrid (2016).

Table Captions:

Table I. Analyzed samples and their SEY parameters. The basic sample structure is defined by capping/nanopillars/substrate. The table collects the presence or absence of each of these components. The capping thickness is around 10 nm. The nanopillars geometry is described as: t-tilted; v-vertical, coal- highly coalesced nanopillars. The deposition rate of the nanopillars is around 10 nm/min, with some deviations associated to the placement of the particle collimator and to the deposition-taking place from only one or both apertures. A Ti layer within the substrate refers to a 2 nm thick adhesion Ti layer. The Au (200) or Ag (200) layers refer to 200 nm thick continuous films. Polished Ag are substrates made from Ag and subsequently polished. The samples Ag Ref. and Au Ref. correspond to standard industry flat smooth samples.

Figure Captions:

Fig. 1: (a) Scheme of the deposition system. (b) Example of sample fabricated without particle collimator. (c) Particle collimator, which has been offset to make visible the substrate below it. (d) Sample fabricated with the particle collimator and deposition from only one aperture (it corresponds to sample #1163 from Table I). (e) Sample fabricated with the particle collimator and alternative deposition from both apertures (sample #1192 from Table I). (f) Cross-sections along and perpendicular to the direction of the flux for a sample fabricated as that in panel (d), *i.e.,* with the particle collimator and alternative deposition from both apertures, but on Si (sample #1182 from Table I).

Fig. 2: (a) SEM images of sample #1192, top-view (left panel) and cross-sections along two perpendicular directions; x (bottom) and y (top). (b) Top view SEM images of Ag nanopillars grown on Ag (sample #1220) and on Au (sample #1219).

Fig. 3: (a) Scheme of the Au-terminated samples; (b) SEY-energy curves of Au-terminated samples with tilted Ag nanopillars fabricated with 13, 26 and 40 min deposition time (samples #1165, #1164 and #1163 in Table I). (c) Low energy region of the above curves. Pink curve corresponds to a flat smooth sample of standard Ag plating from space industry exposed to the air (sample Ag Ref. in Table I).

Fig. 4: (a) SEY-energy curve of a Ag-terminated sample with vertical Ag nanopillars (sample #1220) compared to those of a flat smooth sample of standard Ag plating from space industry exposed to the air and the same reference Ag plating after cleaning with Ar ion bombardment in UHV; (b) SEY-energy curve of an Au-terminated sample with vertical Ag nanopillars (sample #1219) compared to those of a flat smooth air exposed Au sample and the same surface after clean preparation in UHV. The inferior panels show the low energy regions in more detail.

Fig. 5: (a) Relative SEY curves for samples #1220 and #1219. The relative SEY curves are obtained by dividing the SEY curve of those samples with that of the flat smooth samples of Ag and Au exposed to the air, respectively. (b) Relative SEY for the same samples in semi-logarithmic scale.

Fig. 6: (a) Simulation of the multipactor region thresholds with MEST software [36] for infinite parallel geometry and SEY properties of the surface of sample #1220 (blue) and flat smooth Ag plating exposed to the air (red) sample. RF power is proportional to gap voltage squared. (b) Experimental correlation among SEY and Multipactor for various technological prototypes including hypothetical ones with nanopillar coatings of this work. Red symbols, this work; blue symbols, Ref. [7]; violet symbols, Ref. [39]; and green symbols, Ref. [40]. See text.